Sensitivity of model estimates of CME propagation and arrival time to inner boundary conditions

James, L. A., Scott, C. J. ORCID: https://orcid.org/0000-0001-6411-5649, Barnard, L. A. ORCID: https://orcid.org/0000-0001-9876-4612, Owens, M. J. ORCID: https://orcid.org/0000-0003-2061-2453, Lang, M. S. ORCID: https://orcid.org/0000-0002-1904-3700 and Jones, S. R. (2023) Sensitivity of model estimates of CME propagation and arrival time to inner boundary conditions. Space Weather, 21 (4). e2022SW003289. ISSN 1542-7390 doi: https://doi.org/10.1029/2022SW003289 Available at https://centaur.reading.ac.uk/111758/

Space Weather

RESEARCH ARTICLE
10.1029/2022SW003289

Sensitivity of Model Estimates of CME Propagation and Arrival Time to Inner Boundary Conditions

Lauren A. James[1], Christopher J. Scott[1], Luke A. Barnard[1], Mathew J. Owens[1], Matthew S. Lang[1], and Shannon R. Jones[1]

[1]Department of Meteorology, University of Reading, Reading, UK

Key Points:

- Best agreement between model and HI1 data is found for ensemble members that also lead to CME arrival times within 3 hr of observation
- Using data assimilated solar wind speed at the inner boundary showed a 4 hr improvement on CME arrival in this study
- By back-mapping the inner boundary conditions to 8 $R_{\odot}$, we demonstrate a more realistic longitudinal distortion of the CME

Correspondence to:

L. A. James,
l.a.james@pgr.reading.ac.uk

Citation:

James, L. A., Scott, C. J., Barnard, L. A., Owens, M. J., Lang, M. S., & Jones, S. R. (2023). Sensitivity of model estimates of CME propagation and arrival time to inner boundary conditions. *Space Weather*, *21*, e2022SW003289. https://doi.org/10.1029/2022SW003289

Received 14 SEP 2022
Accepted 21 MAR 2023

Abstract Accurately forecasting the arrival of coronal mass ejections (CMEs) at Earth is important to enabling mitigation of the associated space weather risks to society. This is only possible with accurate modeling of the event. To do so, we must understand the propagation of a CME through the heliosphere and quantify the performance of models through comparison with spacecraft observations. For the 12 December 2008 Earth-directed CME event, we compute ensembles using the HUXt solar wind model to analyze CME distortion with a structured solar wind and explore hindcast arrival time error (ATE). By highlighting the impact CME shape has on Root-Mean-Square-Error (RMSE) values, we show that time-elongation profiles of fronts captured by the Heliospheric Imager (HI) instruments onboard NASA's STEREO mission match those of the modeled CME nose and flank and can therefore be used to infer details of the longitudinal extent of the CME. We then show that accounting for CME distortion is important to enable accurate estimates of the CME arrival at Earth. This can be achieved by either using observations of multiple features in HI data to infer CME evolution or mapping the solar wind back to a lower inner boundary to allow CMEs to be distorted close to the Sun. For the event studied we show that these approaches resulted in reduced RMSEs of 0.73° and 0.64° with an ATE of 1 hour and 3 hours respectively.

Plain Language Summary Coronal Mass Ejections (CMEs) are giant erupting magnetic flux ropes from the Sun into space. Upon engulfing Earth, they interact with the near-Earth space environment and result in disruptions to modern electrical infrastructure. Therefore, accurately forecasting CME arrival time at Earth is vital in order to mitigate the risk of space weather. Here, for the 12 December 2008 Earth-directed event, we use a simple-physics solar wind model (HUXt) to explore the distortion that occurs to a CME throughout the journey from the Sun to Earth. Features of the leading edge are tracked from the viewpoint of two spacecraft (STEREO) that are positioned away from the Sun-Earth line and compared to position profiles of bright-light regions pictured by the mission's Heliospheric Imager cameras. By running the HUXt model many times, we explore the relationship between the error of the tracked features and the arrival time error of the hindcast. We find that using multiple features to quantify model performance can improve the arrival time prediction, compared to tracking a single feature. Alternatively, we can account for changes to the CME geometry that occur close to the Sun by ejecting a CME into the model earlier.

1. Introduction

Coronal Mass Ejections (CME) are the major driver of severe space weather impacts (Cane & Richardson, 2000; Gosling, 1993). A CME is a cloud of magnetized plasma moving rapidly away from the Sun, at speeds varying from 300 km s^{-1} to 2,500 km s^{-1} and containing 10^{12}–10^{13} kg of material (Kahler, 1987; Riley & Gosling, 1997). On arrival at Earth, a CME can interact with Earth's magnetosphere, causing short-term changes to the planet's magnetic field, especially if the CME has a southward interplanetary magnetic field component (Arnoldy, 1971; Chao & Chen, 2001; Dungey, 1961). Due to modern civilization's increasing reliance on electrical technologies, society is more vulnerable to the impacts of "space weather." A CME can cause disruption to satellite communications, ground-based power grids and the air travel industry, to name but a few of the detrimental impacts (Cannon, 2013). This highlights the importance of forecast accuracy for Earth-directed CMEs (Barnard et al., 2017; Davies et al., 2012; Hapgood & Thomson, 2018; Möstl et al., 2011; Oughton et al., 2019).

Currently, operational space weather forecasts typically rely on three-dimensional magnetohydrodynamic (3D MHD) models of the solar wind, with CME initial conditions being estimated by analysis of coronagraph data. Such models, like ENLIL (Odstrcil, 2003), are used by NOAA's Space Weather Prediction Center (SWPC) and

the UK Met Office's Space Weather Operation Centre (MOSWOC) to produce deterministic and ensemble forecasts of CME arrival time at Earth (Mays et al., 2015; Pizzo et al., 2011). Due to the computing resources needed by full-physics models to run once, the number of ensemble runs is limited by feasibility (Cash et al., 2015; Lee et al., 2013), with the MOSWOC computing 24 runs in their forecast (Henley & Pope, 2017). Analysis of these forecasts reveals a CME mean arrival time error (ATE) of approximately 13 hr (Iwai et al., 2021; Mays et al., 2015; Riley et al., 2018; Vršnak et al., 2014). An alternative approach used in recent research (e.g., Barnard et al., 2020; Chi et al., 2021) is to use a computationally efficient reduced-physics solar wind model (HUXt, Owens, Lang, Barnard, et al., 2020) to explore parameter space in ensembles with many hundreds to thousands of members. Such ensemble modeling methods can provide both robust uncertainty estimates and probabilistic forecasts (Barnard et al., 2020; Owens & Riley, 2017). It is anticipated that the results from these larger ensembles can ultimately be used to inform targeted ensemble runs using full 3D MHD solar wind models. We here present an analysis of the sensitivity of the HUXt model results to inner boundary conditions. In particular, we determine the accuracy with which HUXt can reproduce multiple CME fronts seen in spacecraft data, aiding our interpretation of such complex observations.

NASA's Solar TErrestrial RElations Observatory (STEREO; Kaiser et al., 2008), launched in late 2006, was designed to further understand the initiation, structure, and the propagation of CMEs, especially Earth-directed events. Consisting of two spacecraft in heliocentric orbits, STEREO-A travels ahead of Earth while STEREO-B lags behind in such a way that they separate from Earth by approximately 22° of ecliptic longitude annually. Both STEREO spacecraft have the same instrument packages that take images of the Sun and solar wind, and in-situ measurements of solar wind plasma and magnetic fields. The remote sensing instrument package Sun–Earth Connection Coronal and Heliospheric Investigation (SECCHI; Harrison et al., 2009; R. A. Howard et al., 2008) can provide information about the three-dimensional structural evolution of a CME. It includes white-light heliospheric imagers (HI; Eyles et al., 2009), white-light coronagraphs (COR) and an extreme ultraviolet imager (EUVI; Wuelser et al., 2004). Together, they observe space from the lower solar atmosphere to beyond 1AU. COR1 and COR2 cover 1.4 solar radii ($R_\odot$)–4 $R_\odot$ and 2 $R_\odot$–15 $R_\odot$, respectively, while HI has a field of view from 15 $R_\odot$ to beyond Earth orbit at 215 $R_\odot$ (R. A. Howard et al., 2008). The HI is composed of two cameras; HI1 and HI2, each with different fields of views that allow a CME to be tracked up to 88.7° elongation from the Sun (Davis et al., 2009; Eyles et al., 2009; R. A. Howard et al., 2008). This mission was the first to observe CME events from multiple viewpoints outside the Sun-Earth line.

The heliospheric imagers rely on Thomson scattering - the process of sunlight being scattered off free electrons (Billings, 1966; Deforest et al., 2013; T. A. Howard & Deforest, 2012; T. A. Howard et al., 2013) to generate their images. Each pixel contains an integration of the light scattered by plasma along that line of sight. As with conventional photography, an HI image is a two-dimensional representation of a three-dimensional structure.

The first major Earth-directed CME was observed by STEREO on 12 December 2008, and has since been the subject of a number of studies (Byrne et al., 2010; Davis et al., 2009; Deforest et al., 2011, 2012; T. A. Howard & Deforest, 2012; Lugaz et al., 2010; Liu et al., 2010; Manchester et al., 2017; Zhang et al., 2019). At this time, STEREO-A and STEREO-B were positioned approximately 42° and −44° from Earth respectively. For STEREO-B, this is a similar viewing geometry to the proposed ESA *Vigil* mission, formerly known as the *Lagrange* mission (Akioka et al., 2005; Thomas et al., 2018; Vourlidas, 2015), therefore, this event represents a useful study of CME observations from such an experiment. One previous study of this event (Davis et al., 2009) assumed the density enhancements seen in HI were discrete substructures within the CME and disturbed solar wind. By using the forecast front arrival times at L1, the behavior of the magnetic and plasma measurements were shown to correlate to the properties of the leading edge, magnetic flux rope, and the core of the CME. Later, by assuming both STEREO spacecraft observed the same feature, a geometric triangulation technique out to 1 AU with prescribed and fixed spherical (Lugaz et al., 2010) and non-spherical fronts (Liu et al., 2010) showed that the direction and distance of the CME could be tracked through the HI field of view to match the L1 in-situ observations. Mapping two-dimensional views seen in HI images to the complex, three-dimensional structures of CMEs is not straightforward. Barnard et al. (2017) demonstrated that assuming a CME retained a simple geometric shape as it propagated through the heliosphere was not consistent with the known uncertainties of the observations. More recently, Scott et al. (2019) suggested that a single three-dimensional leading edge could produce multiple regions (i.e., a nose and a flank) of enhanced Thomson scatter leading to multiple structures within a two-dimensional HI image. For the 12 December 2008 event, it was demonstrated that multiple features seen in

HI images evolved in a way that was consistent with a Kinematically Evolving Flux Rope (Owens et al., 2006) expanding into a structured solar wind.

Here, we use the HUXt model, described below, to make multiple simulations of the 12 December 2008 CME using varying initial conditions to produce elongation profiles and hindcasts. Through comparison with the multiple CME fronts observed by HI, we determine which experiment best reproduces the observations and whether good model performance, determined as a low RMSE in retrospect to all ensemble members, leads to an improved estimate of the CME arrival time at Earth. We test to see how the inclusion of data assimilated solar wind at the inner boundary, the distance of the inner boundary and the assumed uncertainty in the initial parameters impact model output. These will be discussed in more detail in the following section.

2. Techniques

2.1. Solar Wind Data Assimilation

Near-Sun solar wind conditions which serve as the inner boundary conditions to heliospheric models are typically provided by coronal models constrained by the observed photospheric magnetic field (e.g., MAS, WAS, AWSoME; Arge et al., 2004; Holst et al., 2014; Linker et al., 1999). Here, we start with output from the MAS model (Magnetohydrodynamic Algorithm outside a Sphere; Linker et al., 1999) but additionally assimilate the available in situ solar wind observations to provide a more accurate reconstruction of the ambient solar wind conditions.

The Burger Radial Variational Data Assimilation (BRaVDA) solar wind scheme (Lang & Owens, 2019; Lang et al., 2020) calculates an optimal inner boundary condition for a steady state simulation of the equatorial solar wind speed, through the assimilation of in-situ solar wind observations. A perturbation of the MAS model solar wind speed solution for a single Carrington rotation is defined as the prior state at the scheme's 30 $R_\odot$ inner boundary and allowed to propagate out into the simulated heliosphere using the HUX model (Riley & Lionello, 2011, N.B. not to be confused with the time-dependent version, HUXt we use in the study). The solar wind speed error, in units km s^{-1}, is computed at 1 AU between the model and observation from NASA's Advanced Composition Explorer (ACE). By seeking the minimum cost function (sum of prior and observation squared errors, weighted by their relative uncertainties) in the scheme, an optimum inner boundary array is defined as the posterior state. This output from BRaVDA can then be used to define a solar wind speed structure at 30 $R_\odot$ in a heliospheric model, such as HUXt (Owens, Lang, Barnard, et al., 2020) which is done in this study.

In this study, NASA's ACE is used to provide solar wind speed observations. Whilst multi-spacecraft observations are generally desirable to improve accuracy, STEREO-A and STEREO-B observations were not used here due to differences in the solar wind structure measured that are likely the result of the spacecraft heliographic latitude. For this time frame, ACE was positioned at HEEQ latitude of −0.7°, the same as Earth, whilst STEREO-A was below and STEREO-B was above, both positioned at −5.5° and 4.8° HEEQ latitude respectively. A fast stream was measured by STEREO-B but no evidence of this structure was in ACE or STEREO-A data. Thus, this local structure suggests large differences in solar wind structure over relatively small latitudinal ranges about the helio-equator, an issue common during solar minimum (Owens, Lang, Riley, et al., 2020). Instead, in situ data from ACE between 360° and 90° Carrington longitude (i.e., a full Carrington rotation excluding the time at which the CME interacted with the spacecraft) was used in the assimilation. Figure 1 shows the time-series of solar wind speeds at L1 produced by HUXt initialized with the non-data assimilated MAS solar wind conditions and the data assimilated solar wind conditions (BRaVDA), compared to real observations from the ACE spacecraft. Both model outputs produce peaks at the same periods seen in the observation, however, BRaVDA is shown to be better at not overestimating the speed or creating extra peaks. This is most noticeable on 3 December 2008. In the MAS informed HUXt run we note the overestimated peak in speed on 13 December 2008 corresponding to the high-latitude fast steam structure that was identified to only occur in STEREO-B data. This difference between the solar wind speed structures is expected to impact the distortion of the CME which we investigate in Section 5.1.

2.2. HUXt

The Heliospheric Upwind eXtrapolation model with time-dependency (HUXt; Owens, Lang, Barnard, et al., 2020) is a reduced physics 1-D numerical model used to simulate heliospheric conditions and CME propagation. To do this, the complex magnetic equations that are found in full-physics 3-D models, like ENLIL (Odstrcil, 2003), are simplified greatly to the assumption that the plasma is purely radial and behaves as an incompressible and

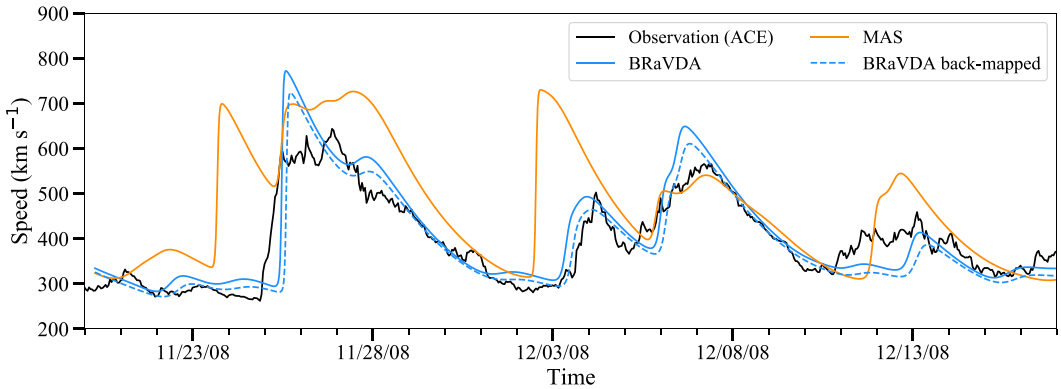

Figure 1. Time series of solar wind speed at L1 for the HUXt model initialized with a non-data assimilated solar wind speed (MAS; orange solid line) and data assimilated solar wind speed (BRaVDA; blue solid line) in comparison to in situ speed measurements from NASA's ACE spacecraft (black solid line). Also displayed is the BRaVDA back-mapped solar wind speed solution at L1 (blue dashed line) which is discussed in Section 5.1. Dates ticks correspond to 00:00 UTC.

inviscid hydrodynamic flow. Modeling in the Earth's latitudinal plane, the heliosphere is represented by a grid of angular resolution 2.8° and radial resolution 1.5 $R_{\odot}$. In the steady-state approximation, this approach was shown to match 3D MHD output (Riley & Lionello, 2011) and has recently been adapted to allow for time-dependent solar wind structure (Owens, Lang, Barnard, et al., 2020). Even with the high level of physical approximation, HUXt can replicate the outwards movement of plasma to beyond 1 AU within 6.4% accuracy of the full-physics model, validated against 40 years' worth of data and the HelioMAS model (Owens, Lang, Barnard, et al., 2020; Riley et al., 2001). Due to these simplifications, the time for a single run of HUXt takes a fraction of a second on an average desktop computer, significantly reduced compared with the full-physics models. The computational efficiency of this model enables the computation of many-member ensembles, as has been done by Barnard et al. (2020).

Within HUXt, CMEs are introduced as a velocity pulse at the inner boundary. The properties of this pulse are determined with information about the source latitude and longitude, width, speed, and thickness derived from cone-model fits to coronagraph images (Millward et al., 2013). Through the thickness parameter required for HUXt setup, which initializes the radial extent of the inserted CME structure, the subsequent deceleration rate of a CME can effectively be changed, essentially by altering the momentum of the CME (Owens, Lang, Barnard, et al., 2020). A CME of zero thickness is a spherical perturbation, whilst larger values produce more of a "sausage" shape. In HUXt, the CME shape is composed of multiple grid cells adjacent to each other, with the shape of the boundary being restricted by the grid resolution. In order to track the CME disturbance through the model, the boundary of a CME is defined as where the velocity difference per a grid-cell is greater than 20 km^{-1} compared to the ambient (i.e., no CME) solar wind solution.

2.3. Ghost Fronts

To bring out dynamic features in HI images, it is common practice to take a running-difference of the images, wherein the previous image is subtracted from the current one to reveal finer detail. In doing so, static and slowly varying features are removed and any changes between HI images appear as bright (increased intensity) and dark (decreased intensity) features. A bright feature that forms a coherent shape is classified as a front. Two nearly identical leading CME fronts are frequently observed in such HI images that are separated by a few degrees of elongation (Scott et al., 2019). Such a feature is also seen for the 12 December 2008 CME, as shown in Figure 2.

It has been shown that there can be a correspondence between the position of the outer front and the pile-up of plasma ahead of the CME (Pant et al., 2016). Shock fronts are produced when the speed of a CME eruption is significantly greater than the ambient solar wind, however, there are occasions where a "ghost front" is observable but there is no in-situ evidence of a leading shock. The CME of 12 December 2008 is one such example (Scott et al., 2019). It is also possible that multiple CME fronts observed in HI data represent different structural features of the same CME, for example, the upstream disturbance, the leading edge and the flux rope (Davis et al., 2009; Möstl et al., 2011). More recently Scott et al. (2019) demonstrated that for the 12 December CME, where the two fronts contained similar latitudinal structure in HI images, the fronts were consistent with the location of the

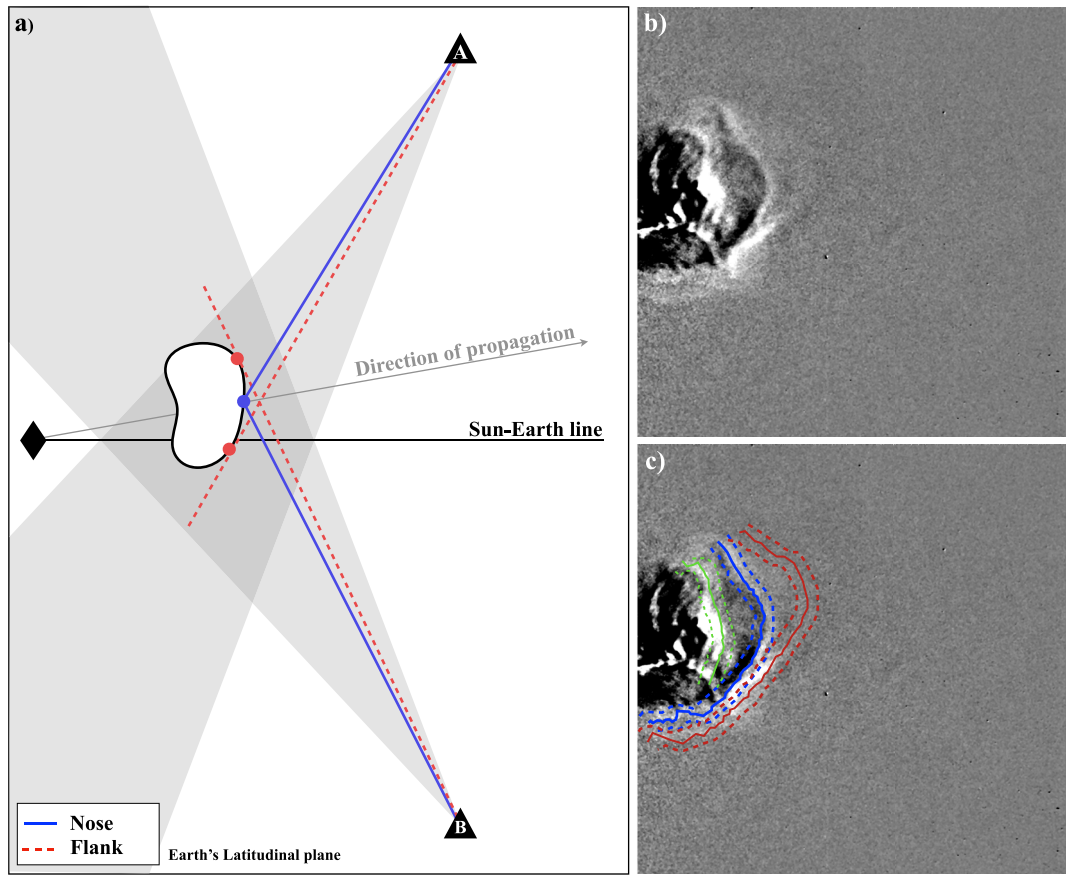

Figure 2. (a) Schematic of the "ghost front" theory Scott et al. (2019) for the December 12th CME, showing the leading edge features that are assumed detectable as bright regions in HI1 data. A CME is traveling away from the Sun (diamond) along the gray line. Observations from the spacecraft (triangles, labeled A and B for the respective STEREO spacecraft) are taken in the HI1 field of view (gray-shaded regions). The tangent of greatest elongation is the flank, identified by the red dots and dashed lines. The nose is indicated by the blue dot and solid lines. (b) An example of a running-differenced Heliospheric Imager image taken from STEREO-B on 13 December 2008. The Sun is positioned on the left of the image and the Earth is positioned on the right. (c) The same image as (b) but now the fronts have been highlighted. The solid line is the average position and the dashed line is the uncertainty. Red is the outermost front, followed by blue and then pale green closest to the Sun. Only the two outermost fronts are of interest for the "ghost front" theory. Thus, the color of these two fronts corresponds to the feature color in the schematic.

leading edge (or "nose") and flank of a single CME front. This we call the "ghost front theory" and is the focus of this study. This previous work concluded that the cause of the "ghost front" was not due to the Thomson sphere as they were observed at elongations smaller than the sphere. In their interpretation, Scott et al. proposed that the CME flank corresponded to the outer front in HI1 images (an enhanced line-integrated signal being returned from the extended feature along the flank) while the pile-up of material ahead of the CME nose resulted in an enhanced signal at slightly lower elongations. It is this secondary front that was denoted as the "ghost" front.

Thomson scattering is vital in being able to understand how CMEs are seen in HI images. The intensity of scattered light in each pixel of an HI image is proportional to the density of free elections integrated along that line of sight as a function of distance from the observer. Features can therefore appear bright in an HI image for a number of reasons. For example, the leading edge surrounding the nose of the CME is likely to appear bright due to the localized increase in plasma density (e.g., Kwon & Vourlidas, 2018) as the plasma accumulates perpendicular to the direction of propagation. An approximation of this region is given by the position of the CME nose, specifically where the CME front lies along the line of propagation. The tangent to the leading edge (i.e., the flank of the CME) can also appear bright due to the cumulative plasma density integrated along the extended line of sight. Thus two bright fronts can be seen in HI images, each resulting from light scattered from different regions of the same front. Figure 2a shows a schematic of the "ghost front" theory for a CME heading earthwards between both

STEREO spacecraft, similar to the 12 December 2008 event. Within HI1 field of view (i.e., early in the CME propagation) the eastern flank is observed from STEREO-A and the western flank is observed by STEREO-B whilst the nose is observed by both STEREO-A and STEREO-B. This "ghost front" model has been applied in the work of Chi et al. (2021) to simulate bright features within CME images. It was shown to be consistent with observations over a range of latitudes. This suggests that measuring the elongation difference between "ghost fronts" can help us determine the longitudinal shape and/or width of a CME from a single spacecraft. Further, there has been a suggestion that using both the nose and the flank to optimize HI1 fitting could improve the forecasting abilities of CMEs at L1/Earth (Barnard et al., 2020; Hinterreiter et al., 2021).

3. Case Study: 12 December 2008 CME

In COR1, the CME was first observed at a radial distance of 7.9 $R_\odot$ at 10:37 UTC on 12 December 2008. Later the event was also captured by HI1, first at a radial distance of 34 $R_\odot$ at 20:49 UTC and was tracked throughout the instrument's field of view. Many techniques have been developed to reconstruct CMEs using coronagraph data, such as the CME Analysis Tool (CAT) used by SWPC (Millward et al., 2013), geometric localisation (Koning et al., 2009), and equal masses (Colaninno & Vourlidas, 2009). By averaging these methods, Scott et al. (2019) concluded that this CME propagated along a solar longitude of $10° \pm 4°$ and latitude $9° \pm 2°$ (HEEQ coordinates) with a speed of 380 km s^{-1} whilst close to the Sun. Further, CME reconstruction using HI1 data suggested an increased radial speed of 497 km $s^{-1} \pm 63$ km s^{-1} throughout the distances observed.

This CME was tracked through the HI1 field of view using the same interface as used with Solar Storm Watch (Barnard et al., 2017). By identifying bright fronts within an image and taking the radial distance of these features where they cross the Earth's latitudinal plane, the elongation angle of each feature was measured. After repeating this for all HI images, a time-elongation profile was produced. We can see the time-elongation profiles for the features of the 12 December 2008 CME in Figure 6a, where two fronts were identified in STEREO-A data and three fronts from STEREO-B. These profiles were also included in the work by Scott et al. (2019), however, only two features were identified within STEREO-B's HI images. In the Solar Stormwatch tracking tool, users were asked to track the position of "ghost fronts" and hence were limited to identifying two features in HI1. In a case where more than two front features were present, such as the 12 December 2008 case, then it was possible for inconsistency between the fronts being tracked between users. The images were processed to allow the data to be categorized into more than two fronts. Now, we find the "inner front" to have a less-noisy time-elongation profile, similar to the profiles seen by STEREO-A. The third feature (shown in green, Figure 2c) projects at a lower elongation. This front can be associated with the highly dense core of the CME, as has been concluded in previous studies of this event (Byrne et al., 2010; Davies et al., 2009). Since we are only considering the outermost CME front in this work, we exclude the time-elongation profile of the third front in our analysis. Traditionally, J-maps were used to extrapolate the trajectory profile of CMEs by identifying sharp changes in white-black boundaries of features that extended throughout the HI1 and HI2 field of view (Davies et al., 2009). By obtaining the direction and speed of the CME, we could estimate Earth's arrival. It has been identified that this method could lead to considerable uncertainties since J-maps use an average position angle used to construct the maps, resulting in CME features appearing fainter at greater elongations (Barnard et al., 2017). Whilst for this reason we do not use J-map to produce the time-elongation profile, we demonstrate how the profiles obtained from the Solar Stormwatch technique correspond to J-map features in Figure 3.

From ACE data, seen in Figure 4, we analyze the CME's arrival at Earth. We interpret the enhancement in solar wind speed at 07:00 UTC $\pm$ 1 hr on 16 December 2008 as the arrival of the compressed solar wind ahead of the CME, just under 4 days from the first COR observation. The solar wind speed increases from approximately 330 km s^{-1} at arrival to 370 km s^{-1} several hours later, along with an associated enhancement in ion density. It becomes clear that these features are indeed associated with a CME when, a few hours later, the magnetic field rotates—in this case southwards—indicating the arrival of the magnetic structure. This observed arrival time is consistent with other studies (Davis et al., 2009; Deforest et al., 2013; Zhang et al., 2019).

4. Method

4.1. Simulating Time-Elongation Profiles

Through the HUXt model, we produce time-elongation profiles for CME features, where the elongation angle is the angle between the Sun-observer-feature. For the "ghost front" theory, we are interested in tracking the flank and nose of the leading edge. In the projected plane, the point at which the leading edge intercepts the radial line of

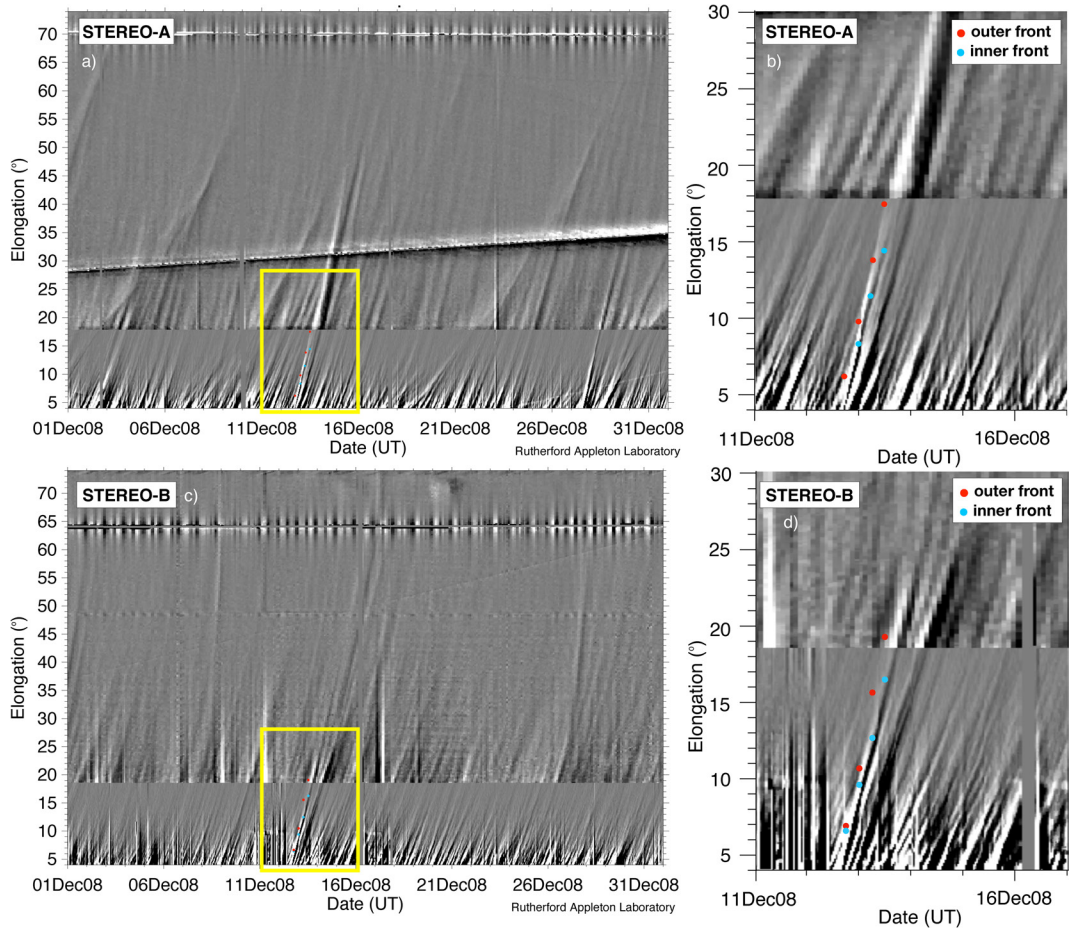

Figure 3. J-maps of the Heliospheric Imager field of view from the view of STEREO-A (top row) and STEREO-B (bottom row). December 2008 data is displayed in (a and c) with the time period corresponding to the CME event encased in the yellow outlined box. This time period is zoomed in for (b and d). For a number of observational time periods 6 hours apart, we overlay the elongation angle that was determined by the Solar Stormwatch front tracking technique for the outer front (blue dot) and inner front (red dot). J-maps were obtained from Rutherford Appleton Laboratory.

propagation is classified as the nose position. The radial line of propagation is equal to the source longitude of the CME. As we use a solar wind speed model, we are unable to specifically identify the position of the dense region in the vicinity of the CME nose, and hence use the reasonable approximation that this corresponds to the point on the front perpendicular to the CME radial speed (described within the paper as the "nose"). This approximation contributes to the uncertainty in the time-elongation profile of the nose. The tangent of the leading edge in respect of the observer which generates the largest elongation angle identifies the flank. For each model time step, the position and elongation angle of the features are found and recorded. Throughout the propagation, the position of the tangent will approach the nose from the far flank before switching to the flank closest to the observer at large elongations, assuming there is no extreme distortion to the CME shape. As a result, the time-elongation profiles of the nose and flank would be expected to merge at some point, and then separate again.

We compare the modeled time-elongation profile to the HI1 observation on the Sun-Earth line. This constraint means we do not track the CME to the point where the nose and flank profiles merge, therefore, we are confident the flank time-elongation profile identified corresponds with the furthest flank from the observer. It is worth noting that this technique is limiting; for an extreme viewing geometry where the furthest flank is not clearly identifiable then the merge point may occur in the HI1 field of view. To quantify the model's performance to simulate the HI1 data, we measure the Root-Mean-Square-Error (RMSE) between the model and observations for each feature. We combine the errors for the flank and nose from both STEREO spacecraft as a single error measurement to represent the total error of the model run.

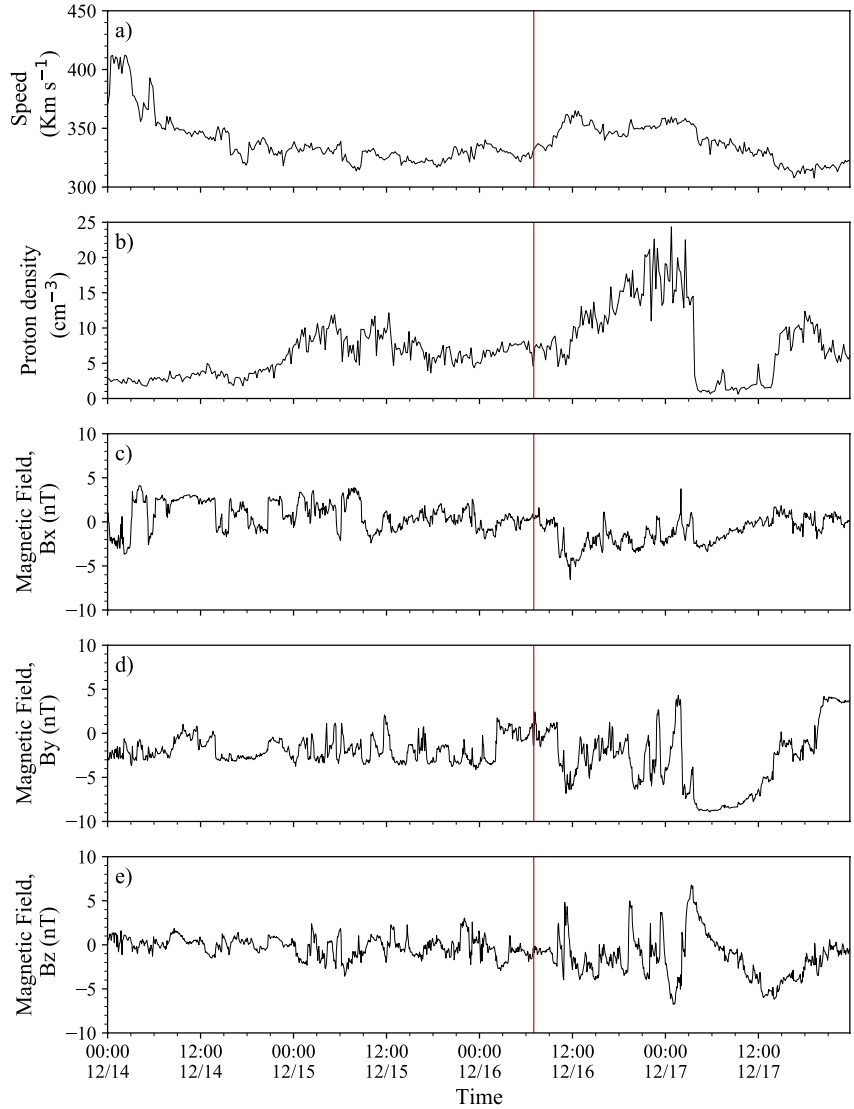

Figure 4. Solar wind data from NASA's ACE spacecraft; (a) the solar wind radial speed, (b) the proton concentration, (c–e) show the heliospheric magnetic field (in GSE coordinates). The red vertical line highlights the CME arrival time, as estimated from an enhancement in solar wind speed. (Source: https://cdaweb.gsfc.nasa.gov/cgi-bin/eval1.cgi.)

4.2. CME Propagation Ensemble

The deterministic run is a single run of a model where the initial conditions are informed by estimates of the parameter, based on observations, and ignoring the value uncertainty. It is one possible outcome of the model, but with confidence that this set of initial conditions is credible. Hence, in ensemble modeling the parameter space of initial conditions is centralized around the deterministic run. Whilst a likely outcome, the deterministic run does not explore the sensitivity of the model to the uncertainty and accuracy of the initial conditions. In our case, the CME initial parameters have an associated uncertainty that we can explore through an ensemble which perturbs these conditions.

In an ensemble, we compute 201 members (200 randomly perturbed members and 1 deterministic member) where the cone CME initial conditions vary as a random, uniform distribution from the deterministic values where the parameter space of the initial condition uncertainties are informed from coronagraph observations. Each ensemble member undergoes the above technique to create time-elongation profiles of the flank and nose and quantifies the accuracy to resemble the HI1 observations. Thus, the ensemble members can be ranked according to RMSE to seek which members best perform. The arrival time of the leading edge at L1 is also recorded for each ensemble member.

Table 1
Overview of Initial Conditions Variables Used for Each Experiment

Model run name	Inner Boundary ($R_\odot$)	Speed (km s^{-1})	Longitude (∘)	Latitude (∘)	Width (∘)	Thickness ($R_\odot$)	Earth's Carrington longitude	Solar wind solution
Experiment 1	30	497 ± 63	10 ± 4	9 ± 2	42 ± 6	5 ± 2	67.966	BRaVDA
Experiment 2	30	497 ± 126	10 ± 8	9 ± 4	42 ± 12	5 ± 4	67.966	BRaVDA
Experiment 3	8	600 ± 100	10 ± 4	9 ± 2	42 ± 6	16.9 ± 2	63.363	BRaVDA
Experiment 4	8	600 ± 200	10 ± 8	9 ± 4	42 ± 12	16.9 ± 4	63.363	BRaVDA

Note. Value and uncertainty (if applicable) of the inner boundary radial distance, CME speed, CME source location, CME full width, CME thickness, Earth's Carrington longitude at the start of the experiment and the solar wind scheme are displayed.

By determining the relation between RMSE and arrival time error (ATE), we can determine if the HI observations contain any information that could be used to improve the estimated arrival time at Earth. To detect if there is a gain to using the "ghost front" theory, we repeat the analysis of ensemble results using the flank time-elongation profiles only, similar to the work of Barnard et al. (2020). For this, the model performance is quantified from the addition of the flank RMSE from both spacecraft only.

4.3. Experiment Variations

There are other inner boundary conditions that can be altered in HUXt which could significantly impact the outputs. In this study, we investigate two alterations: the location of the model's inner boundary; and the magnitude of the assumed uncertainties in the initial CME observations. By taking combinations of these inner boundary alterations, a total of four ensembles (from here we refer to these as experiments) are presented here:

1. CME launched from 30 Rs with parameters perturbing across the estimated uncertainty from coronagraph observations.
2. CME launched from 30 Rs with parameters perturbing across double the estimated uncertainty from coronagraph observations.
3. CME launched from 8 Rs with parameters perturbing across the estimated uncertainty from coronagraph observations.
4. CME launched from 8 Rs with parameters perturbing across double the estimated uncertainty from coronagraph observations.

The cone CME initial condition values and associated uncertainty used in each experiment can be found in Table 1.

4.3.1. Lowering the Inner Boundary of the Model

CMEs have been shown to be accelerating in the initial stages of the propagation up to distances greater than 30 $R_\odot$ (Manchester et al., 2017). The acceleration is not primarily due to the interaction with the ambient solar wind, but, the CME's magnetic energy within the flux-rope driving it forward up to 20 $R_\odot$ (Subramanian & Vourlidas, 2007). The HUXt model does not account for such CME acceleration, but as the inner boundary is typically taken to be 30$R_\odot$, as is the case with the MAS model, this is not a major issue. However, injecting a CME with a geometrically simple shape into the model at 30 $R_\odot$ does not account for any distortion the CME may have undergone while propagating out from the initial coronagraph observations (at 8 $R_\odot$ where the CME appears to have a more regular structure). With the lack of magnetic field in HUXt CMEs (or other representations of cone model CMEs), it is important to ensure the kinematics of a CME in the earlier stages of propagation are represented by other means when using a lower inner boundary.

First, in order to initialize the ambient solar wind at 8 $R_\odot$, the solar wind must be back-mapped to this location from the 30 $R_\odot$. We must consider changes in solar wind acceleration and solar longitude, resulting from solar rotation during the transit time, T, taken for this radial movement to occur between the two boundaries. Riley and Lionello (2011) stated a solar wind acceleration term based on MHD simulations as

$$accV(r) = \alpha V_0 \left[1 - \exp\left(\frac{-(r - r_0)}{r_H}\right)\right], \quad (1)$$

where an acceleration term $\alpha = 0.15$ and the scale height $r_H = 50$ $R_\odot$ produced results in agreement with the HelioMAS model. This equation is used to compute the solar wind speed at the lower boundary, V(8 $R_\odot$), from the solar wind speed at 30 $R_\odot$, V(30 $R_\odot$). T is then given by

$$T = \int_{8R_\odot}^{30R_\odot} \frac{1}{V} dr, \tag{2}$$

where:

$$V(r) = V_0 + accV(r). \tag{3}$$

Using the information derived from these above equations, the change of solar longitude, $\Delta\phi$, can be calculated by

$$\Delta\phi = 2\pi \frac{T}{T_{syn}}, \tag{4}$$

where T_{syn} is the sidereal rotation period of the Sun. Since a structured solar wind is used, there are a range of different transit times and hence longitudinal changes between 30 $R_\odot$ and 8 $R_\odot$. This back-mapping method ignores any stream interaction that takes place. The final step in the process interpolates the output on the HUXt's longitudinal grid spacing.

A cone CME will also alter in size significantly between these radial distances, whereby the CME radius will increase as the event expands throughout its propagation. As a result of the CME radius being smaller at a lower inner boundary, we must conserve the momentum of the event which can be done through the thickness parameter. Ultimately, we aim to simulate a CME from 8 $R_\odot$ that will obtain similar parameters at 30 $R_\odot$ to those we used to initialize the model at the same radial distance. To ensure the total radial length, that is, the distance between the leading edge and the tailing edge, of the CME is kept constant then the following equation must be true

$$2R_{30} + \tau_{30} = 2R_8 + \tau_8 \tag{5}$$

where R is the CME radius of the spherical ends and τ is the thickness, together making the initial "sausage" shape of the CME, and the subscript tells us the initial height of the CME (in units $R_\odot$). With a reduced CME radius at 8 $R_\odot$, we require a greater initial thickness than seen at 30 $R_\odot$ to compensate. The radius of the spherical ends for a CME can be calculated using

$$R = r_0 tan(\lambda) \tag{6}$$

where r_0 is the initial height of the CME and λ is the half-width angle of the CME. By substitution, we can find the equivalent thickness of the CME at the lower inner boundary using

$$\tau_8 = 2 \times 30 tan(\lambda) + \tau_{30} - 2 \times 8 tan(\lambda). \tag{7}$$

For the 12 December 2008 event, we calculate that for a CME launching from 8 $R_\odot$ with a half-width of 21° a thickness of 16.9 $R_\odot$ is required. Assuming the thickness and width are independent variables, the thickness uncertainty remains ± 2 $R_\odot$ when lowering the inner boundary. All other parameters used to define the CME remain unchanged, especially since an initial height of 8 $R_\odot$ is more representative of the chronograph estimate region.

Since we cannot model the initial CME acceleration with HUXt, we simulate this CME acceleration by initializing the model with a speed greater than observed at 30 $R_\odot$ when using a lower inner boundary. Using CME parameters estimated from coronagraph observations, a small set of runs was carried out in which only the initial CME speed is changed between runs. After exploring a large range of initial speeds (300–1,200 km s^{-1}), a local minimum in RMSE for HI1 measurements is found to occur at approximately 600 ± 100 km s^{-1} for all features tracked. Hence, we use this value to define the CME initial speed at the 8 $R_\odot$ boundary. Since the HUXt model simulates CME propagation as the radial outflow of speed only, no shock is created by increasing the speed. The model runs continue to use COR observations made at the radial distance of this lower boundary to describe the source location and longitudinal width of the CME.

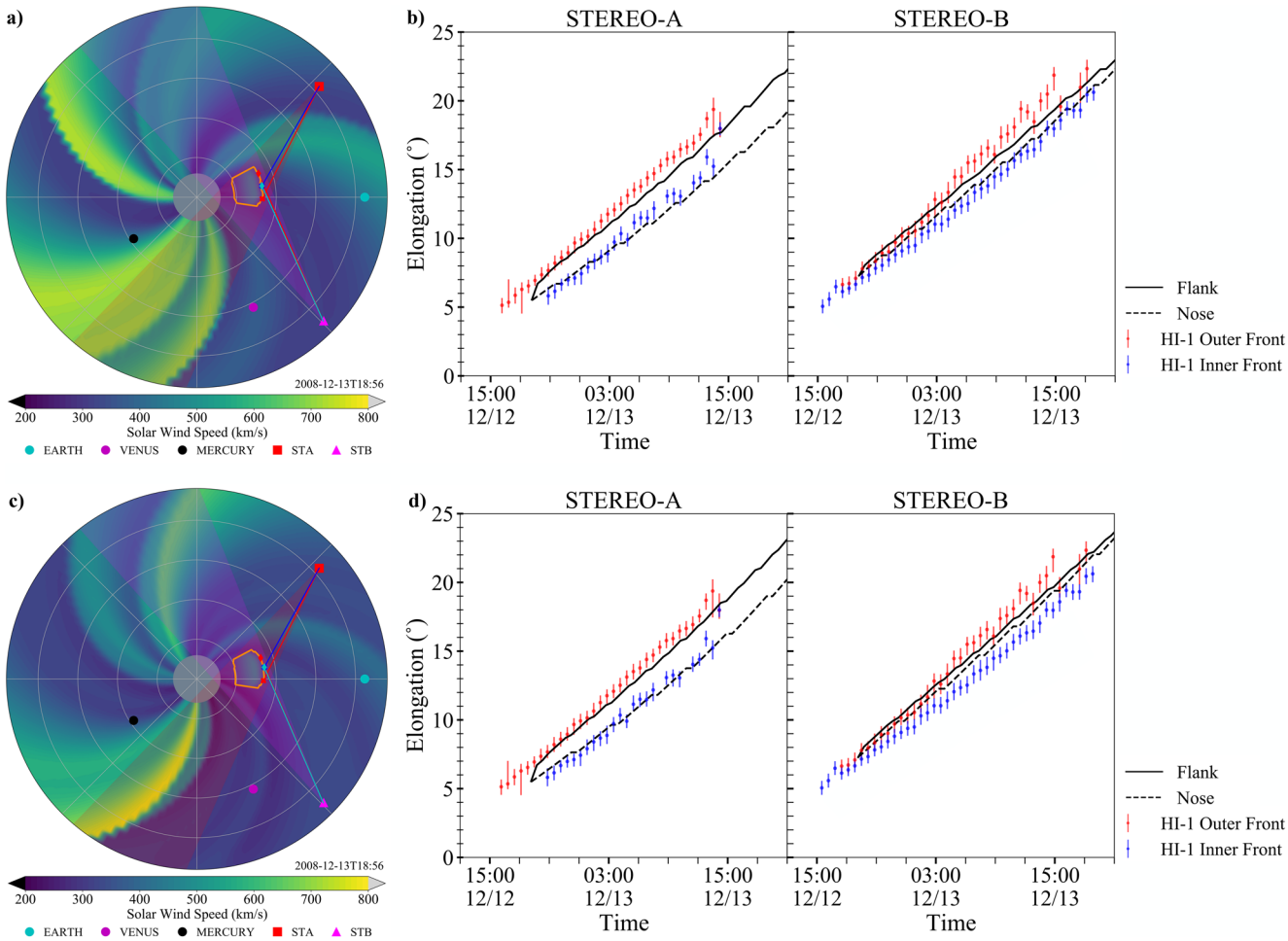

Figure 5. Comparison of HUXt output when run with different solar wind schemes. The top panel shows the MAS non-data assimilated solar wind scheme results. The bottom panel shows the BRaVDA data assimilated solar wind scheme results. The 24-hr solution in Earth's latitudinal plane is displayed in (a and c), showing a CME's interaction with the solar wind structure. The structured solar wind is shown by the background color, whilst the CME edge is identified by the orange-outlined shape. The HI1 field of view is marked as a translucent, triangular shaded region expanding from the spacecraft. For this timestamp, the nose position is indicated by the blue cross/cyan diamond whilst the flank position is marked by the red cross/red diamond along the CME leading edge. Markers for Earth, STEREO, Venus, and Mercury positions are also included. (b and d) show time-elongation plots measured from the position of STEREO-A and STEREO-B for the leading edge nose (black dashed) and flank (black solid) throughout the HI1 field of view. HI1 observations are shown by colored error bars.

4.3.2. Ensemble Parameter Spread

We want to test if the quoted uncertainties of the coronagraph fit were adequate for capturing the breadth of potential outcomes. This is done by allowing the cone CME initial conditions to randomly perturb with uniform distribution (a) among the given parameter uncertainty and (b) among twice the given parameter uncertainty.

5. Results and Discussion

5.1. Modeling the Solar Wind Speed: BRaVDA or MAS?

Earlier in Section 2.1, we explored the difference in the solar wind structure near Earth for CR2077 where by HUXt propagated inner boundary speed conditions from MAS and BRaVDA. In summary, it was found that the data assimilated scheme was better at recreating the speed structures observed by ACE, especially for the duration and maximum speed of fast streams. Now we expand the analysis to explore the impact these solar wind speed schemes have on a CME. We initialize a cone CME from a 30 $R_{\odot}$ inner boundary using coronagraph estimated parameters. Figure 5 shows the CME that has undergone 2-day of distortions in Earth's latitudinal plane as well as the time-elongation profiles of the nose and flank feature through the HI1 field of view.

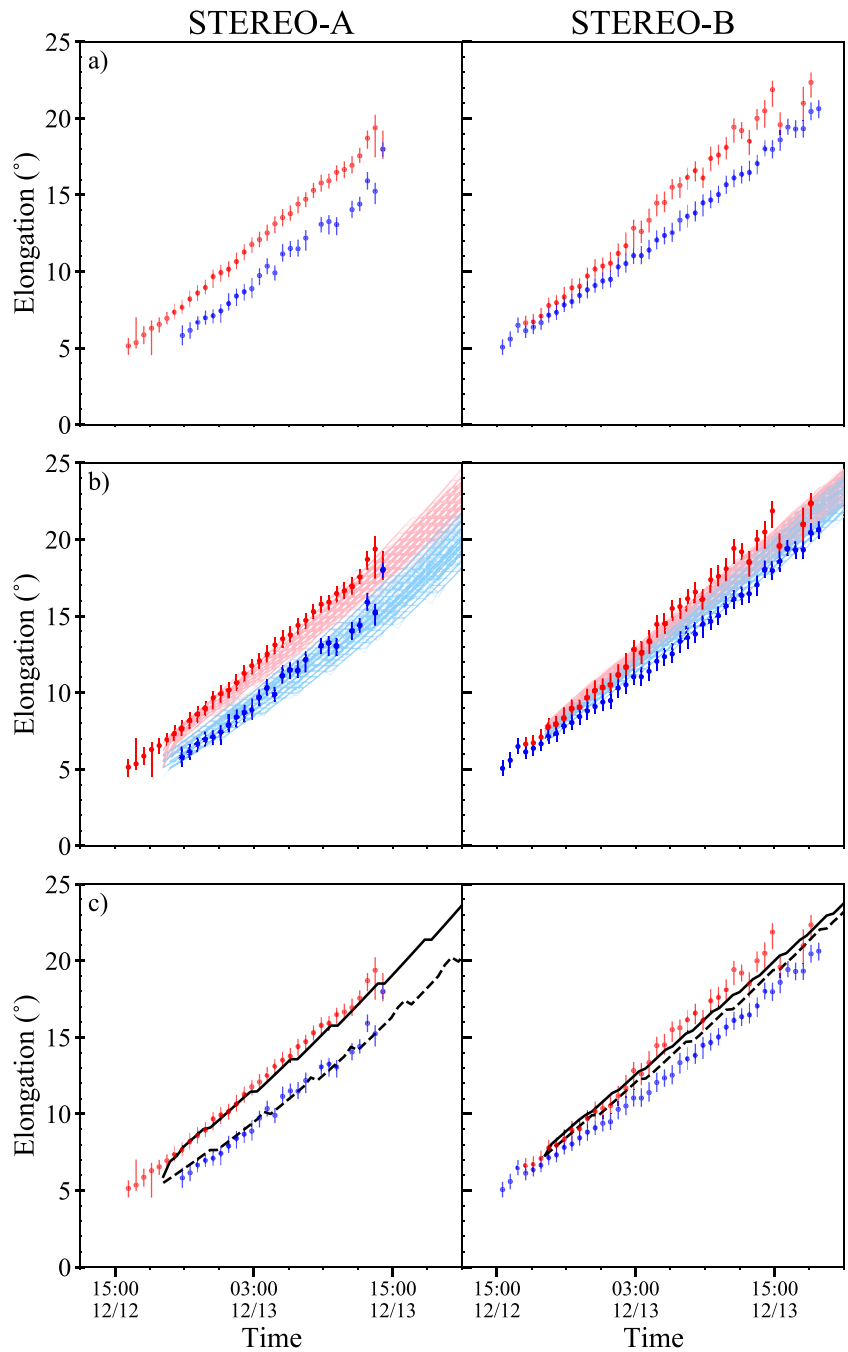

Figure 6. Time-elongation profiles for Experiment 1, with HUXt modeling CME propagation from 30 $R_{\odot}$ inner boundary, measured from the position of STEREO-A (left column) and STEREO-B (right column). Top row: error bar profiles of the leading two dense-plasma fronts seen in Heliospheric Imager (HI) data, measured using the Solar StormWatch technique. Middle row: Modeled data showing the profiles of the nose (pale blue) and flank (pale red) from the 201-member ensemble overlaid with HI data error bar. Bottom row: The profiles of the "best-fit" member with minimized RMSE error of the nose and flank from both spacecraft, overlaid with HI data error bars.

In the top row, we see the MAS initialized case. For this non-data assimilated solution, we find that the time-elongation profile of the nose and flank throughout the HI1 field of view agree well with STEREO-A and STEREO-B observations, obtaining an RMSE of 0.91° and 0.81° respectively. The combined RMSE from both spacecraft is 0.86°. In the bottom row, we show the BRaVDA initialized case, and similarly, the time-elongation profiles also fit well with the observations. For this case, we obtain an RMSE value of 0.68° for STEREO-A,

0.93° for STEREO-B, and 0.83° for both spacecraft. The improvement in recreating STEREO-A observations but not STEREO-B in the latter case can be explained by the leading edge distortion seen in the HUXt plane plots. Both model runs were initialized with the same CME parameters from a 30 $R_\odot$ inner boundary, therefore, these variations are due to the differences in solar wind speed.

In the BRaVDA initialized run we find the CME has maintained a similar curved leading edge structure to its initialized state. The ambient solar wind which the eastern side of the CME is distorting with is estimated as a mildly faster stream than its non-DA counterpart and, as a result, we see the nose at a greater radial distance at this given time. Therefore, from the viewpoint of both STEREO spacecraft, we measure greater elongations at each time step, producing a profile series with a greater gradient. This is visible in Figures 5e and 5f as the nose profiles agrees with more data points in the STEREO-A HI1 field of view and produces a lower RMSE meanwhile STEREO-B yields less agreement. Accordingly, we find this large difference in the quantified error.

In contrast, the MAS initialized run causes the western flank of the CME to be dragged forward with the fast stream creating a flatter leading edge. This impacts the time-elongation profiles seen from STEREO-B whereby the flank will obtain greater elongation measurements than the nose, especially later in the time series. And this is observed in Figure 5b whilst also improving the fit to the observations, resulting in a lower RMSE for STEREO-B. However, earlier we noted that this fast stream seen in the MAS solar wind speed solution is due to a high-latitude fast stream which was not measured by ACE and, therefore, likely less representative of the case study when we are modeling in Earth's latitudinal plane. Despite this, it highlights the importance of understanding CME distortion caused by interaction with solar wind streams for accurately reproducing HI1 observations.

From these results, we choose to only use the BRaVDA scheme to inform the HUXt model inner boundary speed conditions for the ensemble experiments. To support this, we find the hindcast arrival at L1 for the CME in both model runs. For the MAS solar wind speed, the CME arrives at 12:30 UTC ± 34 min on 16 December 2008 (5.5 hr after observed arrival) with a speed of 328 km s^{-1}. Meanwhile, for BRaVDA solar wind speed the CME arrives at 07:53 UTC ± 34 min on 16 December 2008 with a speed of 353 km s^{-1}. Only the data assimilated scheme produces a hindcast that falls within the observation uncertainty of the CME arrival time (07:00 UTC ± 1 hr) and approximate arrival speed of 370 km s^{-1} as seen in Figure 4.

5.2. Constraining Models Using Ghost-Front Features

In Figure 6 we show the development of simulating time-elongation profiles that reasonably reproduce the profiles of tracked fronts within HI1 imagery. In Figure 6a, we show the observed time-elongation profiles seen by STEREO HI1 (more details of how this data was obtained are included in Section 3). In Figure 6b, we show all HUXt simulated profiles from the 201-member ensemble of Experiment 1 (modeling CME from 30 $R_\odot$ with parameters varying within coronagraph observed estimates; Table 1) overlaid with the HI1 observations. In line with the assumptions of the "ghost front" theory, the flank profiles are portrayed in red and the nose profiles in blue to match the HI1 observations these profiles should correspond with. From this ensemble, we show the best-fit time-elongation profile for the nose and flank as seen from both STEREO spacecraft—that is, the model run that produced the lowest RMSE—in Figure 6c. For this model run, from the perspective of STEREO-A the modeled profiles agree with the front elongations fairly well (0.60° RMSE). The flank appears to fit best with the simulated profile agreeing with the error of the HI1 observed fronts, meanwhile, the nose feature doesn't perform quite as well. However, the gradient of these features is in good visual agreement. On the other hand, from the perspective of STEREO-B, the separation between the nose and flank is narrower than seen in the observations. Here we see the gradient of the flank's time-elongation profile is less than observed, with many of the observations differing from the simulations by more than can be explained by uncertainties. The model nose elongation agrees with the points better and therefore we find an RMSE of 0.75°. Collectively, this model run agrees with the observations with an RMSE of 0.69°.

The narrower difference between nose and flank time-elongation profiles produced by the model suggests that it is not capturing the CME distortion accurately enough. More precisely, the radius of curvature of the CME front is too small. One explanation could be that we have used an insufficient range over which the initial parameters of the CME were allowed to vary in the ensemble. As a result, the best combination of CME initial conditions is not computed. We later test this by allowing the initial CME conditions to vary by up to twice the quoted parameter uncertainties. Another reason could be that a significant distortion of the CME occurs before 30 $R_\odot$. Despite this "best-fit" model run agreeing with the HI observation better than the deterministic run, we find that it obtains a

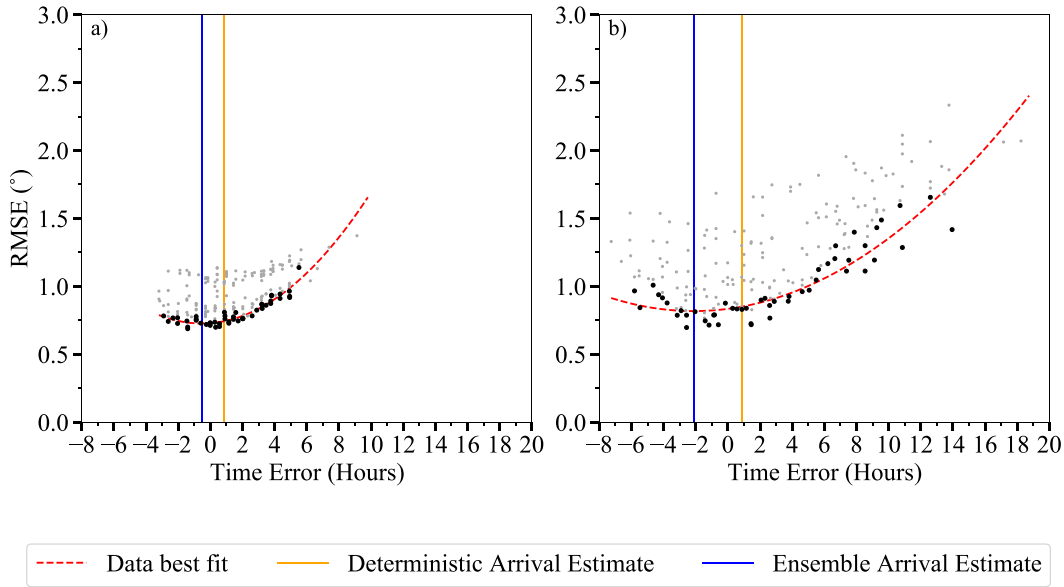

Figure 7. Scatter plots of time-elongation profile RMSE values against arrival time error for each model member, shown in gray and black dots. The lowest 25% of data per bin are highlighted by black dots, and a quadratic line of best fit (red, dashed) is fit to these. In these experiments, HUXt is configured with an inner boundary of 30 $R_{\odot}$ with initial conditions allowed to vary with (a) the coronagraph estimated uncertainty and (b) twice the estimated uncertainty.

worse arrival time that is 2 hr 18 min earlier and falls outside the observed uncertainty. Such a result demonstrates the limitation of using HI time-elongation profiles to constrain a CME's evolution as they are essentially degenerate for many combinations of initial CME parameters. So, as you find here, the "best fit" time-elongation profile might correspond to a simulation that poorly reflects the arrival time at Earth.

Further, due to the random nature of the sampling, identifying the experiment member that produces the lowest RMSE may not be representative of the entire ensemble, and as such, it is not sufficient to use this to draw conclusions on the benefit of using "ghost fronts" to constrain propagation modeling. Hence we now explore the correlation between the HI1 elongation RMSE and ATE, as shown in Figure 7 for the experiments modeled from a 30 $R_{\odot}$ inner boundary. Arrival time error is measured as the difference between the observed CME arrival time and the model run's hindcast such that a negative time error corresponds with an early CME arrival and a positive time error corresponds with a late CME arrival. To ensure we investigate the impact of using multiple fronts to constrain the model, we identify a subset of data to represent the members who agree best with the HI1 observations across the range of arrival time. To do this, we bin the members by their ATE with 34-min resolution (HUXt's output time-step in the configuration of this study) to ensure the ensemble distribution continues to be represented. The lowest 25% of data points per bin are then found and used to create the data subset to which a quadratic line of best fit is found. This percentage appears adequate at reducing the number of data points whilst ensuring low-populated bins were still represented, thus, we could identify the relationship over the whole data range. This was important to produce a quadratic curve that was not unintentionally truncated. The x-value that corresponds to the curve trough is assigned as the ensemble arrival time estimate. The uncertainty of the ATE estimate is defined as the x value, which range is formed from the model time output, that corresponds to an RMSE that is significantly different from the RMSE at the local minima. The error of the RMSE values are calculated using 1 standard deviation of the quadratic coefficient uncertainty. In such a way, sharp curves that better define the minimum will have a low uncertainty whilst less well-defined curves have greater uncertainty. This method does not quantify the error associated with each ensemble member model run as a single value like the mean absolute error (Verbeke et al., 2019), but it allows us to evaluate if constraining the model using HI1 data produces a viable estimate. By taking the subset of data like this, we can explore the variation of best-fit RMSE as a function of arrival time while accounting for the noise generated by random sampling of the CME initial conditions. Hence, upon calculating the minimum value of the curve we can analyze the relationship between the quality of fit and the arrival time at L1.

We note the appearance of vertical separation between two data "clusters" for Experiment 1 (Figure 7a), one which is highlighted by the subset of data and the other by the excluded ensemble data. This is only a visual

Table 2
Overview of the Arrival Time Error Results of the Experiments

Model Run Name	Deterministic ATE (hours)	Nose and Flank Ens. ATE (hours)	Flank Ens. ATE (hours)
Experiment 1	0.9 ± 0.6	−0.5 ± 0.2	**−4.4 ± 1.1**
Experiment 2	0.9 ± 0.6	−2.1 ± 0.5	**−11.1 ± 4.9**
Experiment 3	3.3 ± 0.6	2.8 ± 0.5	0.7 ± 0.8
Experiment 4	3.3 ± 0.6	2.9 ± 0.6	1.6 ± 1.0

Note. Deterministic value is computed using a single run of HUXt initialize with the COR-1 parameter estimates. Ensemble (Ens.) ATE is the minimum of the quadratic relation between the HI1 elongation RMSE and arrival time error for the lowest 25% of members, as seen in Figures 7 and 8. Where the number is in bold font, we note that the value falls outside of the ensemble range of ATE values.

identification, therefore we use the term "cluster" loosely to describe an apparent subset of data. Both have similar curved regression and appear to form a local minimum at similar ATE, though one has much higher RMSE values. The cause of the two clusters is yet to be determined, but a plausible explanation is that there is a common sensitivity to one of the initial values between these model runs. For example, a wider or narrower CME can produce time-elongation profiles that are offset from the observations by a few degrees yet the propagation of the nose is not impacted and hence produces an arrival time in agreement with other members. By finding a subset of ensemble members which identify the members with the lowest RMSE value, we can ensure that we only consider those ensemble members that best match with the HI1 data.

For Experiment 1, the scatter produces a curve minimizing at −0.5 ± 0.2 hr which equates to an arrival time before the observed arrival. This is within the observed arrival uncertainty of ±1.0 hr. The result is 1.5 hr before the deterministic hindcast, but since this is only a difference of three model resolution time-step we cannot say that this is a strong improvement on the deterministic hindcast. The RMSE value associated with the curve minimum is 0.73°. We carry out the same analysis for Experiment 2, where the ensemble of CME parameters is generated by randomly sampling from uniform distributions with twice the spread of Experiment 1. We find that the RMSE variation minimizes at −2.1 ± 0.5 hr. This result produces a less accurate arrival time than both the deterministic and Experiment 1 model runs, which is suggested by an increased RMSE value of 0.82° at the minima. From increasing the initial parameter range and maintaining the ensemble size, we note that there is a reduced resolution within the parameter space which may increase the variation in RMSE values between ensemble members. If an ensemble size was large enough, it could be said that Experiment 1 and 2 would find the same local minima. In application, this can be tricky to do as more model runs equate to additional computing time and resources. In a simplified physics model, such as HUXt, then adding more members is feasible if the computer allows it. However, with complex models then large member ensembles are not feasible. Hence, we see operational forecasts use a small number of runs in their ensemble models. As such, we do not desire to increase the number of model runs to ensure the conclusions are the same. Therefore, here we conclude that there is no evidence to support doubling the coronagraph uncertainty estimates as ensemble initial conditions.

If only the flank time-elongation profile (i.e., the outermost CME front detected in HI) is considered, as was done in the work by Barnard et al. (2020), we find that the quadratic curve minimizes at −4.4 ± 1.1 hr with RMSE of 0.90° for Experiment 1 and −11.1 ± 4.9 hr with RMSE of 0.70° for Experiment 2. However, we note these ATE values fall outside of the range of values obtained by the ensemble members (minimum ATE is 03:48 UTC 16 December 2008 and 23:44 UTC 15 December 2008 respectively) highlighting that the outcomes are unreliable estimates. The result for Experiments 1 and 2 are summarised in Table 2. Thus far in the case study, an early CME arrival is estimated when launched from an initial height of 30 $R_\odot$, but the accuracy of the ATE estimate is improved when including CME nose tracking in ensemble modeling.

5.3. Lowering the Model Inner Boundary to 8 $R_\odot$

By reducing the model inner boundary, and thus the CME launch, to the radius at which the CME parameters were estimated, the deterministic hindcast produces an L1 arrival at 10:17 UTC + 34 min on 16 December 2008 with a speed of 334 km s^{-1}. This outcome falls between the two previous deterministic arrival times produced from HUXt with initial height of 30$R_\odot$. When comparing the time-elongation profiles of the nose and flank to the fronts observed in HI1, the RMSE values for STEREO-A, STEREO-B, and both spacecraft are 0.61°, 0.74°, and 0.69° respectively. This equates to an improvement in the RMSE compared with the 30 $R_\odot$ deterministic run by at least 10%.

We analyze the model outputs for Experiments 3 and 4 and display the relationship between the RMSE and ATE in Figure 8. By fitting the curve to the lowest 25% of binned data, we find that the curve minimizes at 2.8 ± 0.5 and 2.9 ± 0.5 hr respectively. There is improvement to the arrival time accuracy compared to the deterministic run. But, no improvment from the ensembles computed from 30$R_\odot$ and now these experiments predict an arrival

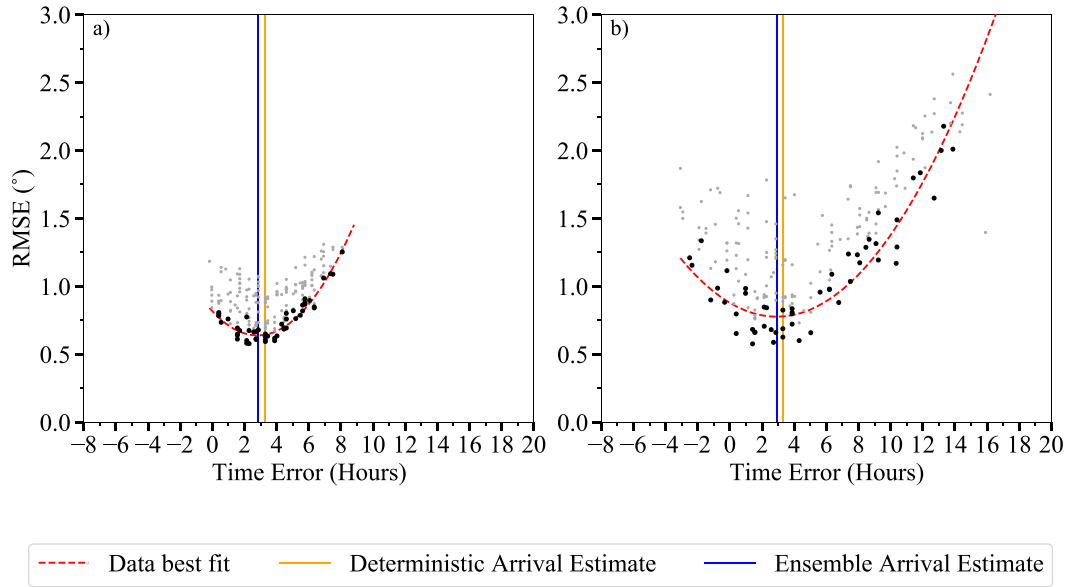

Figure 8. Scatter plots of the time-elongation profile RMSE values and the arrival time error for each model member, shown in gray and black dots. The lowest 25% of data per bin are highlighted by black dots, and a quadratic line of best fit (red, dashed) is fit to these. These plots show (a) Experiment 3 and (b) Experiment 4, where HUXt is configured with an inner boundary of 8 $R_\odot$.

later than observed. But it is interesting to see that despite doubling the range over which the initial parameters can vary in Experiment 4, the fit to the data produces a consistent ATE result. This was not observed in the earlier experiment despite keeping the ensemble size constant, suggesting that by simulating early distortion to the CME then the time-elongation profiles throughout the HI1 field of view are more unique to the model member allowing RMSE values to better indicate the performance of the initial parameters. We see this demonstrated in the figure by a sharper best-fit curve fitting to the data than compared to their counterpart experiment for 30 $R_\odot$. Further, it highlights that the parameter uncertainties based on coronagraph observations are sufficient.

The 8 $R_\odot$ ensemble ATE estimate associates with a lower RMSE value than its 30 $R_\odot$ counterpart; 0.73° drops to 0.64° when using the estimated coronagraph parameter uncertainty (Experiment 3), and 0.82° drops to 0.78° when using twice the estimated uncertainties (Experiment 4). These results highlight again that by allowing the CME to distort before reaching the field of view covered by HI1 then the model can simulate the real data with better accuracy. Whilst this idea is expected of a real CME propagation through the heliosphere, it is important to remember that the simplified HUXt model is replicating the kinematics only and that replicating this in an MHD model may find vastly different outcomes a magnetic fields close to the Sun impacts the CME shape and motion.

Again, we look at the results for a situation where only the flank RMSE is considered. It is found that the curve minimizes at 0.7 ± 0.8 hr for Experiment 3 and 1.6 ± 1.0 hr for Experiment 4, therefore producing a better estimate of the arrival time than using both the nose and flank features. Again, the results for Experiments 3 and 4 are summarised in Table 2. Whilst previous results highlight that the elongation of multiple fronts detected in HI1 data can be replicated using the nose and flank of a CME leading edge, these results here suggest that tracking a single feature may also be sufficient in producing arrival predictions as long as we account for early CME distortion by lowering the inner boundary of the model. The accuracy with which the flank's time-elongation profile evolves from the lower inner boundary may be unique to this case study in which HUXt accurately captures the distortion of a relatively slow-moving event. It would be of interest to find if this outcome is replicated in other CME case studies.

6. Conclusions

We have modeled the 12 December 2008 CME using the HUXt solar wind model with BRaVDA's solar wind speed solution to produce multiple ensemble hindcasts. By using the data assimilated solar wind speed, the L1

CME arrival was found to improve by 4.62 hr in comparison to using non-data assimilated speed from the MAS model, and as a result, produced an estimated arrival time that coincided with the observed CME arrival on 16 December 2008, 07:00 UTC ± 1.0 hr. Through four experiments, we investigate the sensitivity of model inner boundary conditions and the parameter uncertainty using 201-member ensembles. A collective L1 ATE is estimated based on the relationship between the model's ability to simulate HI1 observation of the nose and flank, quantified with an RMSE, and the ATE of the individual members.

From the presented results, it is clear that accounting for CME distortion, at altitudes below the typical lower boundary of solar wind models, is important for accurate modeling. We have demonstrated here that this can be achieved by two methods. One approach is to use the multiple fronts seen in HI1 images to inform us of the position of the nose and flank through the "ghost front" theory assumptions. Thus, we can evaluate the model's performance to simulate the longitudinal distortion by comparing time-elongation profiles of the features and HI1 observations. Allowing the ensemble CME parameters to vary within the uncertainty of coronagraph parameter estimates, we were able to obtain a quadratic function that estimates an L1 arrival time within 1 hour before the observed arrival, although this change when doubled the CME parameter uncertainties. Whilst a very good CME arrival was also produced using the deterministic run, the ensemble techniques produces a more credible result. Using a single feature, in particular the flank, produced an unrealistic result; an ATE which fell outside the ensemble's range.

Alternatively, we can lower the model's inner boundary to recognize distortion to the CME shape before reaching the HI1 field of view. In doing so, the RMSE values of the ensemble members are more varied suggesting the time-elongation profiles better represent the model's sensitivity to the initial conditions. The hindcast estimate is less accurate than method one (approximately 3 hr after observed arrival), however, the ATE is consistent despite allowing ensemble CME parameters to vary within 1× and 2× the uncertainty of coronagraph parameter estimates. Consequently, this indicates a better ATE estimate. On this occasion, evaluating model performance based on the CME flank profile only produced a valid result which estimated a better L1 ATE of no more than 1.6 hr ± 1.0 hr. But this result was associated with the largest RMSE values of all the work presented. Our work suggests that the coronagraph based uncertainties quoted for this CME are indeed adequate as initial conditions for the cone CME. In light of these results, since current magnetohydrodynamic forecast models use a heliospheric inner boundary of approximately 30 $R_{\odot}$, above which most CME acceleration is considered to have already occurred, adopting the tracking "ghost-front" features as a way of constraining forecast models would seem to be the most convenient way of accounting for low altitude distortion of the CME.

Through this work, we have highlighted the available opportunities of the HUXt model to produce ensembles and simulate the near-Sun heliosphere by lowering the inner boundary to produce near-accurate estimated arrivals at L1, despite the reduced physics approach (i.e., plasma is assumed to be purely radial to eliminate the need of complex magnetic equations to describe its motion). It is acknowledged that density measurements in CME modeling are an important aspect for space weather forecasting although it is not available in the current version of HUXt. In the future, it would be beneficial to include solar wind density modeling into ghost-front applications to enhance our confidence that the flank and nose regions tracked in this study do correspond to the dense plasma regions we expect to find at the leading edge of CMEs.

Using HI time-elongation profiles to assess the model performance of CME distortion can be limiting as they can degenerate for many combinations of initial CME parameters. Therefore, estimating the arrival time using a function which describes the ATE and RMSE is more representative of the ensemble, removes noise produced from random sampling and allows us to analyze the impact multiple-front tracking has. This would not be possible if we only seek the single member that produced the best fit for HI1 observations. Adopting a comprehensive systematic sampling approach (where model runs are created for all combinations of input parameters within their uncertainty intervals) would be computationally more expensive but may enable a consistent estimate of the best fit to the ghost-front data. This will be considered in future work.

Of course, we have only considered a single event in this study; a slow-moving CME with a suitable spacecraft position for STEREO to view both flanks simultaneously throughout the HI1 field of view. Further investigations should follow to explore the limitations of the method and find out if these suggested conclusions are consistent across a range of CME events. For fast-moving events, which are more geoeffective, it is also necessary to differentiate between the outer front in the "ghost fronts" theory and shock fronts propagating ahead of the CME. To do this work, we would suggest the use of a robust analysis method of error measurement, as reported by Verbeke

et al. (2019), for a comprehensive comparison of using HUXt against other forecasting models. Furthermore, future missions like ESA's Vigil L5 mission (Akioka et al., 2005; Vourlidas, 2015) may only provide HI observation from one position outside the Sun-Earth line and we cannot currently say if our technique is adequate for this.

Data Availability Statement

The HUXt model used in the research can be downloaded at https://github.com/University-of-Reading-Space-Science/HUXt. HUXt version 1.0 was used in this work, with adjustments made inline with model development to amend functions and include lowering inner boundary functionality. This is published on Zenodo at https://doi.org/10.5281/zenodo.7701930 (James, 2023). Data assimilated solar wind scheme BRaVDA can be accessed from https://github.com/University-of-Reading-Space-Science/BRaVDA or found archived on Zenodo https://doi.org/10.5281/zenodo.4849682 (Lang, 2021), using MAS inputs from http://www.predsci.com/mhdweb/home.php. ACE data is accessible via https://cdaweb.gsfc.nasa.gov. Heliospheric Imager data was accessed from UK Solar System Data Centre at http://www.ukssdc.rl.ac.uk/solar/stereo/data.html and analysed using the Solar Stormwatch front tracking interface. J-maps for December 2008 were downloaded from RAL Space at https://www.stereo.rl.ac.uk/cgi-bin/movies.pl.

Acknowledgments
We are grateful to the STEREO/HI instrument team at Rutherford Appleton Laboratory and the UK Solar System Data Centre for the creation and access to Heliospheric Imager data. We also thank the scientist and CDAWed who contributed to the creation and open access to ACE data. Further appreciation to the Solar StormWatch Team and Zooniverse who developed the front tracking interface which provided the time-elongation profiles essential to this work. L. A. James is funded through STFC studentship ST/T506370/1. C. J. Scott, L. A. Barnard and M. J. Owens are funded by STFC ST/V000497/1. M. J. Owens and M. S. Lang are funded by NERC NE/S010033/1.

References

Akioka, M., Nagatsuma, T., Miyake, W., Ohtaka, K., & Marubashi, K. (2005). The l5 mission for space weather forecasting. *Advances in Space Research*, *35*(1), 65–69. https://doi.org/10.1016/j.asr.2004.09.014

Arge, C. N., Luhmann, J. G., Odstrcil, D., Schrijver, C. J., & Li, Y. (2004). Stream structure and coronal sources of the solar wind during the May 12th, 1997 CME. *Journal of Atmospheric and Solar-Terrestrial Physics*, *66*(15–16), 1295–1309. https://doi.org/10.1016/j.jastp.2004.03.018

Arnoldy, R. L. (1971). Signature in the interplanetary medium for substorms. *Journal of Geophysical Research*, *76*(22), 5189–5201. https://doi.org/10.1029/ja076i022p05189

Barnard, L. A., de Koning, C. A., Scott, C. J., Owens, M. J., Wilkinson, J., & Davies, J. A. (2017). Testing the current paradigm for space weather prediction with heliospheric imagers. *Space Weather*, *15*(6), 782–803. https://doi.org/10.1002/2017SW001609

Barnard, L. A., Owens, M. J., Scott, C. J., & Koning, C. A. (2020). Ensemble CME modeling constrained by heliospheric imager observations. *AGU Advances*, *1*(3). https://doi.org/10.1029/2020av000214

Billings, D. (1966). *A guide to the solar corona*. Academic Press.

Byrne, J. P., Maloney, S. A., McAteer, R. T., Refojo, J. M., & Gallagher, P. T. (2010). Propagation of an Earth-directed coronal mass ejection in three dimensions. *Nature Communications*, *1*, 74. https://doi.org/10.1038/ncomms1077

Cane, H. V., Richardson, I. G., & St. Cyr, O. C. (2000). Coronal mass ejections, interplanetary ejecta and geomagnetic storms. *Journal of Geophysical Research*, *27*(21), 3591–3594. https://doi.org/10.1016/j.jastp.2009.08.005

Cannon, P. (2013). Extreme space weather: Impacts on engineered systems and infrastructures. Retrieved from http://www.raeng.org.uk/news/publications/list/reports/Space_Weather_Full_Report_Final.PDF

Cash, M. D., Biesecker, D. A., Pizzo, V., Koning, C. A. D., Millward, G., Arge, C. N., et al. (2015). Ensemble modeling of the 23 July 2012 coronal mass ejection. *Space Weather*, *13*(10), 611–625. https://doi.org/10.1002/2015SW001232

Chao, J. K., & Chen, H. H. (2001). Prediction of southward IMF Bz. *Geophysical Monograph Series*, *125*, 183–189. https://doi.org/10.1029/GM125p0183

Chi, Y., Scott, C., Shen, C., Barnard, L. A., Owens, M. J., Xu, M., et al. (2021). Modeling the observed distortion of multiple (ghost) CME fronts in stereo heliospheric imagers. *The Astrophysical Journal Letters*, *917*(2), L16. https://doi.org/10.3847/2041-8213/ac1203

Colaninno, R. C., & Vourlidas, A. (2009). First determination of the true mass of coronal mass ejections: A novel approach to using the two stereo viewpoints. *The Astrophysical Journal*, *698*(1), 852–858. https://doi.org/10.1088/0004-637X/698/1/852

Davies, J. A., Harrison, R. A., Perry, C. H., Möstl, C., Lugaz, N., Rollett, T., et al. (2012). A self-similar expansion model for use in solar wind transient propagation studies. *The Astrophysical Journal*, *750*(1), 23. https://doi.org/10.1088/0004-637X/750/1/23

Davies, J. A., Harrison, R. A., Rouillard, A. P., Sheeley, N. R., Perry, C. H., Bewsher, D., et al. (2009). A synoptic view of solar transient evolution in the inner heliosphere using the heliospheric imagers on stereo. *Geophysical Research Letters*, *36*(2), L02102. https://doi.org/10.1029/2008GL036182

Davis, C. J., Davies, J. A., Lockwood, M., Rouillard, A. P., Eyles, C. J., & Harrison, R. A. (2009). Stereoscopic imaging of an Earth-impacting solar coronal mass ejection: A major milestone for the stereo mission. *Geophysical Research Letters*, *36*(8), 1–5. https://doi.org/10.1029/2009GL038021

Deforest, C. E., Howard, T. A., & McComas, D. J. (2012). Disconnecting open solar magnetic flux. *The Astrophysical Journal*, *745*(1), 36. https://doi.org/10.1088/0004-637X/745/1/36

Deforest, C. E., Howard, T. A., & Tappin, S. J. (2011). Observations of detailed structure in the solar wind at 1 AU with STEREO/HI-2. *The Astrophysical Journal*, *738*, 1–12. https://doi.org/10.1088/0004-637X/738/1/103

Deforest, C. E., Howard, T. A., & Tappin, S. J. (2013). The Thomson surface. II. Polarization. *The Astrophysical Journal*, *765*(1), 44. https://doi.org/10.1088/0004-637X/765/1/44

Dungey, J. W. (1961). Interplanetary magnetic field and the auroral zones. *Physical Review Letters*, *6*(2), 47–48. https://doi.org/10.1103/PhysRevLett.6.47

Eyles, C. J., Harrison, R. A., Davis, C. J., Waltham, N. R., Shaughnessy, B. M., Mapson-Menard, H. C., et al. (2009). The heliospheric imagers onboard the stereo mission. *Solar Physics*, *254*(2), 387–445. https://doi.org/10.1007/s11207-008-9299-0

Gosling, J. T. (1993). The solar flare myth. *Journal of Geophysical Research*, *98*(A11), 18937–18949. https://doi.org/10.1029/93ja01896

Hapgood, M., & Thomson, A. (2018). Its impact on Earth and implications for business.

Harrison, R. A., Davies, J. A., Rouillard, A. P., Davis, C. J., Eyles, C. J., Bewsher, D., et al. (2009). Two years of the stereo heliospheric imagers: Invited review. *Solar Physics*, *256*(1–2), 219–237. https://doi.org/10.1007/s11207-009-9352-7

Henley, E. M., & Pope, E. C. (2017). Cost-loss analysis of ensemble solar wind forecasting: Space weather use of terrestrial weather tools. *Space Weather*, *15*(12), 1562–1566. https://doi.org/10.1002/2017SW001758
Hinterreiter, J., Amerstorfer, T., Reiss, M. A., Möstl, C., Temmer, M., Bauer, M., et al. (2021). Why are ELEvoHI CME arrival predictions different if based on STEREO-A or STEREO-B heliospheric imager observations? *Space Weather*, *19*(3), 1–18. https://doi.org/10.1029/2020sw002674
Holst, B. V. D., Sokolov, I. V., Meng, X., Jin, M., Manchester, W. B., Tóth, G., & Gombosi, T. I. (2014). Alfvén wave solar model (AWSOM): Coronal heating. *The Astrophysical Journal*, *782*(2), 782. https://doi.org/10.1088/0004-637X/782/2/81
Howard, R. A., Moses, J. D., Vourlidas, A., Newmark, J. S., Socker, D. G., Plunkett, S. P., et al. (2008). Sun Earth connection coronal and heliospheric investigation (SECCHI). *Space Science Reviews*, *136*(1–4), 67–115. https://doi.org/10.1007/s11214-008-9341-4
Howard, T. A., & Deforest, C. E. (2012). The Thomson surface. I. reality and myth. *The Astrophysical Journal*, *752*(2), 752. https://doi.org/10.1088/0004-637X/752/2/130
Howard, T. A., Tappin, S. J., Odstrcil, D., & Deforest, C. E. (2013). The Thomson surface. III. Tracking features in 3d. *The Astrophysical Journal*, *765*(1), 45. https://doi.org/10.1088/0004-637X/765/1/45
Iwai, K., Shiota, D., Tokumaru, M., Fujiki, K., Den, M., & Kubo, Y. (2021). Validation of coronal mass ejection arrival-time forecasts by magnetohydrodynamic simulations based on interplanetary scintillation observations. *Earth Planets and Space*, *73*, 1–17. https://doi.org/10.1186/s40623-020-01345-5
James, L. A. (2023). Sensitivity of model estimates of CME propagation and arrival time to inner boundary conditions (Version Publication_release_v1.0.0) [Computer software]. Zenodo. https://doi.org/10.5281/ZENODO.7701930
Kahler, S. (1987). Coronal mass ejections. *Reviews of Geophysics*, *25*(3), 663–675. https://doi.org/10.1029/RG025i003p00663
Kaiser, M. L., Kucera, T. A., Davila, J. M., Cyr, O. C. S., Guhathakurta, M., & Christian, E. (2008). The stereo mission: An introduction. *Space Science Reviews*, *136*(1–4), 5–16. https://doi.org/10.1007/s11214-007-9277-0
Koning, C. A. D., Pizzo, V. J., & Biesecker, D. A. (2009). Geometric localization of CMES in 3d space using stereo beacon data: First results. *Solar Physics*, *256*(1–2), 167–181. https://doi.org/10.1007/s11207-009-9344-7
Kwon, R. Y., & Vourlidas, A. (2018). The density compression ratio of shock fronts associated with coronal mass ejections. *Journal of Space Weather and Space Climate*, *8*, A08. https://doi.org/10.1051/swsc/2017045
Lang, M. (2021). University-of-Reading-Space-Science/BRaVDA: BRaVDA (Version v1.0) [Computer software]. Zenodo. https://doi.org/10.5281/ZENODO.4849682
Lang, M., & Owens, M. J. (2019). A variational approach to data assimilation in the solar wind. *Space Weather*, *17*(1), 59–83. https://doi.org/10.1029/2018SW001857
Lang, M., Witherington, J., Turner, H., Owens, M. J., & Riley, P. (2020). Improving solar wind forecasting using data assimilation (pp. 1–29). Retrieved from http://arxiv.org/abs/2012.06362
Lee, C. O., Arge, C. N., Odstrčil, D., Millward, G., Pizzo, V., Quinn, J. M., & Henney, C. J. (2013). Ensemble modeling of CME propagation. *Solar Physics*, *285*(1–2), 349–368. https://doi.org/10.1007/s11207-012-9980-1
Linker, J. A., Mikic, Z., a Biesecker, D., Forsyth, R. J., Gibson, S. E., Lazarus, A. J., et al. (1999). Magnetohydrodynamic modeling of the solar corona during whole sun month. *Geophysical Research Letters*, *104*(A5), 9809–9830. https://doi.org/10.1029/1998ja900159
Liu, Y., Davies, J. A., Luhmann, J. G., Vourlidas, A., Bale, S. D., & Lin, R. P. (2010). Geometric triangulation of imaging observations to track coronal mass ejections continuously out to 1 AU. *The Astrophysical Journal Letters*, *710*, 82–87. https://doi.org/10.1088/2041-8205/710/1/L82
Lugaz, N., Hernandez-Charpak, J. N., Roussev, I. I., Davis, C. J., Vourlidas, A., & Davies, J. A. (2010). Determining the azimuthal properties of coronal mass ejections from multi-spacecraft remote-sensing observations with stereo secchi. *The Astrophysical Journal*, *715*(1), 493–499. https://doi.org/10.1088/0004-637X/715/1/493
Manchester, W., Kilpua, E. K., Liu, Y. D., Lugaz, N., Riley, P., Török, T., & Vršnak, B. (2017). The physical processes of CME/ICME evolution. *Space Science Reviews*, *212*(3–4), 1159–1219. https://doi.org/10.1007/s11214-017-0394-0
Mays, M. L., Taktakishvili, A., Pulkkinen, A., MacNeice, P. J., Rastätter, L., Odstrcil, D., et al. (2015). Ensemble modeling of CMES using the WSA–ENLIL+Cone model. *Solar Physics*, *290*(6), 1775–1814. https://doi.org/10.1007/s11207-015-0692-1
Millward, G., Biesecker, D., Pizzo, V., & Koning, C. A. D. (2013). An operational software tool for the analysis of coronagraph images: Determining CME parameters for input into the WSA-ENLIL heliospheric model. *Space Weather*, *11*(2), 57–68. https://doi.org/10.1002/swe.20024
Möstl, C., Rollett, T., Lugaz, N., Farrugia, C. J., Davies, J. A., Temmer, M., et al. (2011). Arrival time calculation for interplanetary coronal mass ejections with circular fronts and application to stereo observations of the 2009 February 13 eruption. *The Astrophysical Journal*, *741*(1), 34. https://doi.org/10.1088/0004-637X/741/1/34
Odstrcil, D. (2003). Modeling 3-D solar wind structure. *Advances in Space Research*, *32*(4), 497–506. https://doi.org/10.1016/S0273-1177(03)00332-6
Oughton, E. J., Hapgood, M., Richardson, G. S., Beggan, C. D., Thomson, A. W., Gibbs, M., et al. (2019). A risk assessment framework for the socioeconomic impacts of electricity transmission infrastructure failure due to space weather: An application to the United Kingdom. *Risk Analysis*, *39*(5), 1022–1043. https://doi.org/10.1111/risa.13229
Owens, M. J., Lang, M., Barnard, L. A., Riley, P., Ben-Nun, M., Scott, C. J., et al. (2020). A computationally efficient, time-dependent model of the solar wind for use as a surrogate to three-dimensional numerical magnetohydrodynamic simulations. *Solar Physics*, *295*(3), 43. https://doi.org/10.1007/s11207-020-01605-3
Owens, M. J., Lang, M., Riley, P., Lockwood, M., & Lawless, A. S. (2020). Quantifying the latitudinal representivity of in situ solar wind observations. *Journal of Space Weather and Space Climate*, *10*, 8. https://doi.org/10.1051/swsc/2020009
Owens, M. J., Merkin, V. G., & Riley, P. (2006). A kinematically distorted flux rope model for magnetic clouds. *Journal of Geophysical Research*, *111*(A3), 1–8. https://doi.org/10.1029/2005JA011460
Owens, M. J., & Riley, P. (2017). Probabilistic solar wind forecasting using large ensembles of near-sun conditions with a simple one-dimensional "upwind" scheme. *Space Weather*, *15*(11), 1461–1474. https://doi.org/10.1002/2017SW001679
Pant, V., Willems, S., Rodriguez, L., Mierla, M., Banerjee, D., & Davies, J. A. (2016). Automated detection of coronal mass ejections in stereo heliospheric imager data. *The Astrophysical Journal*, *833*(1), 80. https://doi.org/10.3847/1538-4357/833/1/80
Pizzo, V., Millward, G., Parsons, A., Biesecker, D., Hill, S., & Odstrcil, D. (2011). Wang-Sheeley-Arge-Enlil cone model transitions to operations. *Space Weather*, *9*(3), 2. https://doi.org/10.1029/2011SW000669
Riley, P., & Gosling, J. T. (1997). By a fast, high-pressure coronal mass ejection (Vol. *102*).
Riley, P., Linker, J. A., & Mikić, Z. (2001). An empirically-driven global MHD model of the solar corona and inner heliosphere. *Journal of Geophysical Research*, *106*(A8), 15889–15901. https://doi.org/10.1029/2000ja000121
Riley, P., & Lionello, R. (2011). Mapping solar wind streams from the sun to 1 au: A comparison of techniques. *Solar Physics*, *270*(2), 575–592. https://doi.org/10.1007/s11207-011-9766-x

Riley, P., Mays, M. L., Andries, J., Amerstorfer, T., Biesecker, D., Delouille, V., et al. (2018). Forecasting the arrival time of coronal mass ejections: Analysis of the CCMC CME scoreboard. *Space Weather*, *16*(9), 1245–1260. https://doi.org/10.1029/2018SW001962

Scott, C. J., Owens, M. J., de Koning, C. A., Barnard, L. A., Jones, S. R., & Wilkinson, J. (2019). Using ghost fronts within stereo heliospheric imager data to infer the evolution in longitudinal structure of a coronal mass ejection. *Space Weather*, *17*(4), 539–552. https://doi.org/10.1029/2018SW002093

Subramanian, P., & Vourlidas, A. (2007). Energetics of solar coronal mass ejections. *Astronomy and Astrophysics*, *467*(2), 685–693. https://doi.org/10.1051/0004-6361:20066770

Thomas, S. R., Fazakerley, A., Wicks, R. T., & Green, L. (2018). Evaluating the skill of forecasts of the near-Earth solar wind using a space weather monitor at l5. *Space Weather*, *16*(7), 814–828. https://doi.org/10.1029/2018SW001821

Verbeke, C., Mays, M. L., Temmer, M., Bingham, S., Steenburgh, R., Dumbović, M., et al. (2019). Benchmarking CME arrival time and impact: Progress on metadata, metrics, and events. *Space Weather*, *17*(1), 6–26. https://doi.org/10.1029/2018SW002046

Vourlidas, A. (2015). Mission to the Sun-Earth l5 Lagrangian point: An optimal platform for space weather research. *Space Weather*, *13*(4), 197–201. https://doi.org/10.1002/2015SW001173

Vršnak, B., Temmer, M., Žic, T., Taktakishvili, A., Dumbović, M., Möstl, C., et al. (2014). Heliospheric propagation of coronal mass ejections: Comparison of numerical WSA-ENLIL+Cone model and analytical drag-based model. *The Astrophysical Journal - Supplement Series*, *213*(2), 213. https://doi.org/10.1088/0067-0049/213/2/21

Wuelser, J.-P., Lemen, J. R., Tarbell, T. D., Wolfson, C. J., Cannon, J. C., Carpenter, B. A., et al. (2004). *Euvi: The STEREO-SECCHI extreme ultraviolet imager*. In (Vol. 5171, p. 111). SPIE. https://doi.org/10.1117/12.506877

Zhang, M., Feng, X. S., & Yang, L. P. (2019). Three-dimensional MHD simulation of the 2008 December 12 coronal mass ejection: From the sun to interplanetary space. *Journal of Space Weather and Space Climate*, *9*, 1–17. https://doi.org/10.1051/swsc/2019034